PHYSICAL REVIEW E **108**, 025204 (2023)

Collisional-energy-cascade model for nonthermal velocity distributions of neutral atoms in plasmas

Keisuke Fujii[*]
Oak Ridge National Laboratory, Oak Ridge, Tennessee 37831-6169, USA

(Received 14 October 2022; revised 23 June 2023; accepted 14 July 2023; published 11 August 2023)

Nonthermal velocity distributions with much greater tails than a Maxwellian have been observed for radical atoms in plasmas for a long time. Historically, such velocity distributions have been modeled by a two-temperature Maxwell distribution. In this paper, I propose a model based on collisional energy cascade, which has been studied in the field of granular materials. In the collisional energy cascade, a particle ensemble undergoes energy input at the high-energy region, entropy production by elastic collisions among particles, and energy dissipation. For radical atoms, energy input may be caused by the Franck-Condon energy of molecular dissociation or charge-exchange collision with hot ions, and the input energy is eventually dissipated by collisions with the walls. I show that the steady-state velocity distribution in the collisional energy cascade is approximated by the generalized Mittag-Leffler distribution, which is a one-parameter extension of the Maxwell distribution. This parameter indicates the degree of the nonthermality and is related to the relative importance of energy dissipation over entropy production. This model is compared with a direct molecular dynamics simulation for simplified gaseous systems with energy input, as well as some experimentally observed velocity distributions of light radicals in plasmas.

DOI: 10.1103/PhysRevE.108.025204

I. INTRODUCTION

Nonthermal velocity distributions have been observed for neutral atoms in plasmas for a long time [1–5]. Spectral profiles with much larger wings than a Maxwellian have been frequently observed. While this is typically most apparent in hydrogen atomic emission lines, as their Doppler broadening is easily observed with a conventional high-resolution spectrometer, similar nonthermal velocity distributions have been reported for other atoms [6]. The origin of such a nonthermal velocity distribution has been attributed to generation processes of energetic atoms, such as Franck-Condon energy obtained through molecular dissociation, and charge-exchange collision with hot ions [6–11]. Many groups have empirically approximated these nonthermal energy distributions by a sum of two (or more) Maxwell distributions [2,4,6]. However, the two-temperature model does not consider the relaxation of energetic atoms. Furthermore, this model does not have a direct connection to a physical quantity, and thus it is difficult to extract knowledge from the observed nonthermal velocity distribution. Some Monte Carlo simulations also have reproduced the observed nonthermal velocity distribution [11–13], but it is not always applicable as all the physics quantities should be known beforehand for the system of interest.

In this paper, I propose to model such nonthermal velocity distributions of neutral atoms focusing more on the energy dissipation or relaxation processes than the energy input processes. In particular, the application of the collisional-energy-cascade model is proposed, which has been studied in the field of granular gaseous. This model has been originally proposed by Ben-Naim *et al.* [14–16], where they consider the three essential properties in the system: (1) a heat source in the high-energy limit, (2) energy dissipation, and (3) elastic collision among particles. They point out that, under this condition, the steady-state velocity distribution has a power-law tail in the high-velocity region.

For radical atoms in plasmas, the heat source may be caused by the Franck-Condon energy of molecular dissociation or by charge-exchange collision with hot ions, while this input energy is eventually dissipated by the wall collisions. Elastic collision among atoms may randomize the kinetic energy. This similarity suggests the applicability of this collisional-energy-cascade model to the velocity distribution of radical atoms in plasmas, which is the purpose of this paper. Although the steady-state solution of this model has not been reported previously, in this paper I show that this is approximated by the generalized Mittag-Leffler (GML) distribution, which is a one-parameter extension of the Maxwell distribution. The GML distribution has no analytic representation except for a few special cases, but its Laplace transform can be simply written by $\mathcal{L}_{f_{\mathrm{GML}}}(s) = \int_0^\infty f_{\mathrm{GML}}(E)\, e^{-sE} dE = [1 + 2D^{-1}(\langle E\rangle_\alpha s)^\alpha]^{-D/2\alpha}$. Here $\langle E\rangle_\alpha > 0$ is the energy scale and D is the spatial dimension of the system. $0 < \alpha \leqslant 1$ is the stability parameter related to the relative importance of the dissipation process, and $\alpha = 1$ corresponds to the thermal system, where the GML distribution reduces to the Maxwell distribution. Thus, α can be seen as a dimensionless parameter representing the degree of nonthermality. In this paper, this steady-state solution will be compared with a direct molecular dynamics simulation, as well as some experimental observations.

---

[*] fujiik@ornl.gov

This paper is organized as follows. In Sec. II, the kinetic theory of gaseous particles with energy dissipation and its connection to the GML distribution is discussed. In Sec. III B, the direct molecular simulations for a simplified situations will be presented. In Sec. IV, several previous measurements for the velocity distribution of atoms in plasmas will be presented and compared with a GML distribution.

II. THEORY

In this section, a theory leading the GML distribution is discussed. Also, a numerical computation of the GML distribution, as well as the velocity distribution corresponding to the GML energy distribution, is described.

A. Derivation of GML energy distribution for Maxwell gases

Consider an isotropic and spatially uniform ensemble of particles undergoing elastic collisions (i.e., no energy dissipation at this point) in D-dimensional space. A Maxwell-type interparticle interaction is assumed for now. Particle ensembles with other interactions will be discussed in Sec. II C. With a Maxwell interaction, the kinetic energies of two colliding particles, E_1 and E_2, can be thought of as random samples from the energy distribution $f(E)$. For many collision systems, the postcollision energy E_1' can be written by the following form:

$$E_1' \leftarrow xE_1 + yE_2, \tag{1}$$

where $x, y \in [0, 1]$ are random numbers following the probability distribution $p(x, y)$, which are determined by the collision geometry, such as the scattering angle and the relation between the relative and center-of-mass velocities. In a steady state, E_1' should also follow $f(E)$.

Several forms of $p(x, y)$ have been proposed. The simplest example of valid $p(x, y)$ is the so-called *diffuse* collision [17,18], where after the elastic collision the two energies will be completely randomized, i.e., no memory effect of precollision energies,

$$p(x, y) = B\left(x \middle| \frac{D}{2}, \frac{D}{2}\right)\delta(x - y), \tag{2}$$

where $B(x|a, b) = x^{a-1}(1 - x)^{b-1}/B(a, b)$ is beta distribution with beta function $B(a, b) = \int_0^1 x^{a-1}(1 - x)^{b-1}dx$ and $\delta(t)$ is Dirac's delta function. The *p-q* model [17,19], which takes the memory effect into account, as well as its linear superposition, also give a valid $p(x, y)$ (see Appendix for the detailed discussion of this probabilistic representation). Note that the symmetry of the elastic collision leads $p(x, y) = p(1 - y, 1 - x)$ as a general property, which results in $\int (x + y)p(x, y)dx\,dy = 1$ for any valid $p(x, y)$.

In the steady state, Eq. (1) can be written in the following form with the Laplace transform of the energy distribution $\mathcal{L}_f(s) \equiv \int_0^\infty f(E)e^{-sE}dE$:

$$\mathcal{L}_f(s) = \int \mathcal{L}_f(xs)\mathcal{L}_f(ys)\, p(x, y)\, dx\, dy. \tag{3}$$

With any valid $p(x, y)$, the steady-state distribution converges to a Maxwell distribution $\mathcal{L}_f(s) = [1 + 2D^{-1}\langle E\rangle s]^{-D/2}$ according to Boltzmann's H-theorem. Here $\langle E\rangle$ is the mean kinetic energy of the system.

Let us additionally consider a system with energy dissipation. It is assumed that, by this dissipation process, a particle loses its kinetic energy by the fraction of $1 - e^{-\Delta}$ (with $\Delta \geqslant 0$). The energy transfer to the surrounding walls can be considered as this dissipation process, but another process can be also considered, such as inelastic collisions among macroscopic particles. Similarly to Eq. (1), a recursive relation with this dissipation can be constructed as follows:

$$E_1' \leftarrow \begin{cases} e^{-\Delta}E_1, & \text{with probability } \xi \\ xE_1 + yE_2, & \text{with probability } 1 - \xi \end{cases}, \tag{4}$$

where ξ is the rate of this dissipation process relative to the elastic collision. The Laplace representation of Eq. (4) at the steady state is

$$\mathcal{L}_f(s) = \xi\mathcal{L}_f(e^{-\Delta}s) + (1 - \xi)\int \mathcal{L}_f(xs)\mathcal{L}_f(ys)\, p(x, y)\, dx\, dy. \tag{5}$$

Here it is implicitly assumed that constant energy injection exists in the high-energy limit, so that the system will eventually arrive at a nontrivial steady state [14]. As a particle having infinitely large kinetic energy is assumed to be injected into the system at an infinitely small rate, this effect does not appear in Eq. (5). In an actual system, the energy of the injected particle should be finite. This finite-energy effect will be discussed later.

Consider the first two orders of $\mathcal{L}_f(s)$. From the normalization condition $\mathcal{L}_f(0) = 1$, it can be written that $\mathcal{L}_f(s) \approx 1 - (\langle E\rangle_\alpha s)^\alpha$ in the small-$|s|$ region, with $0 < \alpha \leqslant 1$. Here $\langle E\rangle_\alpha$ is the energy scale of the distribution. By substituting this into Eq. (5), we obtain

$$1 = (1 - \xi)\int (x^\alpha + y^\alpha)p(x, y)\, dx\, dy + \xi e^{-\alpha\Delta}. \tag{6}$$

This indicates that $\alpha = 1$ is the necessary and sufficient condition for the nondissipative system, i.e., $\Delta = 0$ or $\xi = 0$. With a finite energy dissipation, $\alpha < 1$.

Note that the lowest-order approximation, $\mathcal{L}_f(s) \approx 1 - (\langle E\rangle_\alpha s)^\alpha$, corresponds to an assumption of $f(E)$ in the large-E region, i.e., either $f(E) \approx E^{-\alpha-1}/(\langle E\rangle_\alpha)^\alpha\Gamma(1 - \alpha)$ if $\alpha < 1$ or $f(E) \approx \exp(-E/\langle E\rangle_\alpha)/\langle E\rangle_\alpha$ if $\alpha = 1$. This asymptotic form is consistent with the argument by Ben-Naim *et al.* [14–16], where the steady-state velocity distribution of inelastic gases has a power-law tail, and the index of the power-law tail converges to a finite value (which is 2 for Maxwell gases) at the no-dissipation limit ($\alpha \to 1$). Furthermore, our theory explains how this tail converges to the Maxwell distribution at the thermal limit [observe that $\Gamma(\epsilon)^{-1} \approx \epsilon$ with $0 < \epsilon \ll 1$].

At the large-s limit, with $\Delta \ll 1$, $\mathcal{L}_f(s)$ asymptotically behaves $\approx 2D^{-1}(\langle E\rangle_\alpha s)^{-D/2}$ at the steady state. By combining with its lowest-order approximation, we find that the GML distribution [20–22],

$$\mathcal{L}_f(s) \approx \left[1 + \frac{2}{D}(\langle E\rangle_\alpha s)^\alpha\right]^{-D/2\alpha}, \tag{7}$$

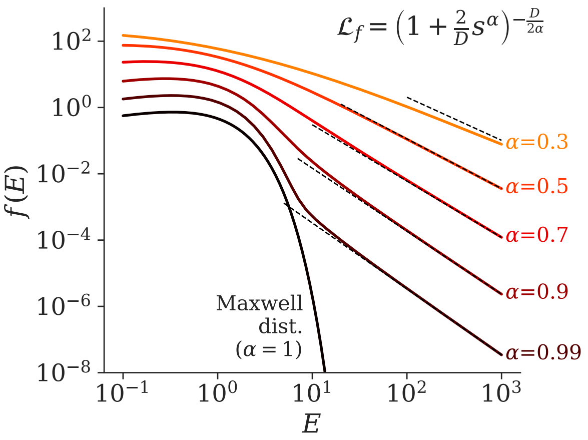

FIG. 1. The GML distribution with several values of α with $\langle E\rangle_\alpha = 1$ and $D = 3$. The power-law tail $E^{-\alpha-1}/\Gamma(1-\alpha)$ is shown by dotted lines. Appropriate offsets are introduced for clarity.

is the simplest approximation of the steady-state solution of Eq. (4). The GML distribution naturally reduces to the Maxwell distribution at $\alpha \to 1$.

B. Numerical evaluation of GML distribution

Although the GML distribution has no analytical forms except for few special cases, some efficient numerical computation methods have been proposed [20–22]. The GML distribution, $f_{\rm GML}(E|\alpha, D, \langle E\rangle_\alpha) = \mathcal{L}^{-1}[(1 + 2(\langle E\rangle_\alpha s)^\alpha/D)^{-D/2\alpha}]$ can be written as a mixture representation of the exponential function;

$$f_{\rm GML}(E|\alpha, D, \langle E\rangle_\alpha) = \frac{1}{\pi\langle E\rangle_\alpha}\left(\frac{D}{2}\right)^{\frac{1}{\alpha}} \times \int_0^\infty \frac{\exp\left[-y\left(\frac{D}{2}\right)^{\frac{1}{\alpha}}\frac{E}{\langle E\rangle_\alpha}\right]\sin\left[\pi\frac{D}{2}F_\alpha(y)\right]}{[y^{2\alpha}+2y^\alpha\cos(\pi\alpha)+1]^{D/4\alpha}}dy, \tag{8}$$

where $F_\alpha(y)$ is defined as follows:

$$F_\alpha(y) = 1 - \frac{1}{\pi\alpha}\cot^{-1}\left[\cot(\pi\alpha) + \frac{y^\alpha}{\sin(\pi\alpha)}\right]. \tag{9}$$

Observe that Eq. (8) is the form of the weighted mixture of an exponential function, i.e., $\int_0^\infty \exp(-cE)w(c)dc$, where c is the scale and $w(c)$ is its weight (weight can be negative in this case).

Figure 1 shows the GML distribution for several values of α with $D = 3$ and $\langle E\rangle_\alpha = 1$. Here the function values of the GML distribution are computed by integrating Eq. (8) numerically. As expected from the small-$|s|$ dependence, it has a power-law tail, $E^{-\alpha-1}/\Gamma(1-\alpha)$. The dotted lines in the figure are these power-law functions. The GML distribution approaches this power-law tail in the large-E region.

The GML distribution is the distribution of the total kinetic energy E. With a spectroscopic measurement, only the velocity distribution along a particular axis is observed. In D = 3-dimensional space, this velocity distribution can be evaluated by substituting $E = m(v_x^2 + v_y^2 + v_z^2)/2$ and integrating it over v_x and v_y by taking the statistical weight of free space into account, where v_x, v_y, and v_z are the velocity components in the three-dimensional space and m is the mass of the particle. Since only the term depending on E in Eq. (8) is $\exp(-cE)$ with $c = y(\frac{D}{2})^{\frac{1}{\alpha}}/\langle E\rangle_\alpha$, the integration of this term is sufficient.

Consider the energy distribution $g(E|c) = c\exp(-cE)$ in three-dimensional space. As the statistical weight of the space is $\sqrt{2mE}$ in the energy domain, the distribution of v_z is

$$g(v_z|c) = c\int_{-\infty}^{\infty}\exp(-cE)\frac{1}{\sqrt{2mE}}dv_x dv_y = \frac{1}{2}\sqrt{\frac{c}{2m}}\,\Gamma\left(\frac{1}{2}, c\frac{v_z^2}{2m}\right), \tag{10}$$

where $\Gamma(s,x) = \int_x^\infty t^{s-1}e^{-t}dt$ is the lower incomplete gamma function. By substituting Eq. (10) into Eq. (8), i.e., by replacing the term $\exp(-y(D/2)^{1/\alpha}E/\langle E\rangle_\alpha)$ in Eq. (8) by $g(v_z|y(D/2)^{1/\alpha}/\langle E\rangle_\alpha)$, we obtain the velocity distribution of particles with their total kinetic energy following the GML distribution.

C. GML distributions for non-Maxwell gases

The above discussions can be approximately extended to particles having other interparticle interactions. For example, the collision rate of hard spheres is proportional to $E^{\lambda/2}$ with $\lambda = 1$ while neutral atomic gases show Van der Waals interaction, where $\lambda = 1/3$ [23,24]. For such systems, we may consider the weighted distribution, $\hat{f}(E) = E^{\lambda/2}f(E)/Z$, with the normalization constant Z. Based on an approximation $(E_1 + E_2)^{\lambda/2} \approx (E_1E_2/\langle E\rangle_\alpha)^{\lambda/2}$, which is valid if $|\lambda| \ll D$, this weighting approximately represents the energy dependence of the collision rate. Although this weighting changes the statistical weight of the D-dimensional space from $\propto E^{D/2-1}$ to $\propto E^{(D+\lambda)/2-1}$, the Laplace transform of its weighted distribution at the steady state is approximated by the GML distribution, $\mathcal{L}_{\hat{f}}(s) = [1 + (D + \lambda)(\langle E\rangle_\alpha s)^\alpha/2]^{-(D+\lambda)/2\alpha}$.

For the $\lambda \neq 0$ case, the energy distribution can be obtained by simply multiplying $E^{-\lambda/2}$ to Eq. (8),

$$f_{\rm GML}(E|\alpha, D, \langle E\rangle_\alpha, \lambda) \propto \frac{1}{\pi\langle E\rangle_\alpha}\left(\frac{D+\lambda}{2}\right)^{\frac{1}{\alpha}} \times \int_0^\infty \frac{E^{-\frac{\lambda}{2}}\exp\left[-y\left(\frac{D+\lambda}{2}\right)^{\frac{1}{\alpha}}\frac{E}{\langle E\rangle_\alpha}\right]\sin\left[\pi\frac{D+\lambda}{2}F_\alpha(y)\right]}{[y^{2\alpha}+2y^\alpha\cos(\pi\alpha)+1]^{(D+\lambda)/4\alpha}}dy. \tag{11}$$

The corresponding velocity distribution can be obtained by replacing $g_\lambda(E|c) = cE^{-\lambda/2}\exp(-cE)$ by

$$g_\lambda(v_z|c) = \frac{c^{\lambda/2}}{2}\sqrt{\frac{c}{2m}}\,\Gamma\left(\frac{1-\lambda}{2}, c\frac{v_z^2}{2m}\right). \tag{12}$$

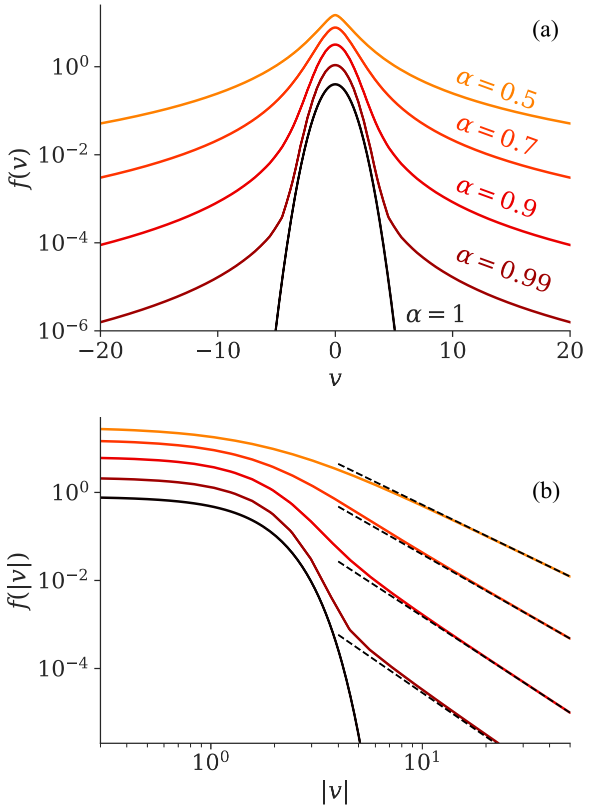

FIG. 2. Velocity distributions corresponding to GML energy distributions. $D = 3$ and $\lambda = 1/3$ are used. Distributions with several values of α are shown with vertical offsets for clarity. The distribution with $\alpha = 1$ is a Gaussian. The distribution with $\alpha \lesssim 1$ is similar to a Gaussian in the central part but has much larger wings. With a smaller value of α, the wing fraction is larger. Panel (a) is a semilog plot and panel (b) is a log-log plot. The dotted lines in (b) show the power-law distribution $\propto |v|^{-2\alpha-\lambda-1}$.

To summarize, the velocity distribution corresponding to the energy distribution $E^{-\lambda/2} f_{\mathrm{GML}}(E)$ can be written as

$$f(v_z) \propto \int_0^\infty g_\lambda\{v_z|y[(D+\lambda)/2]^{1/\alpha}/\langle E\rangle_\alpha\} \times \frac{\sin\left[\pi\frac{D+\lambda}{2}F_\alpha(y)\right]}{[y^{2\alpha}+2y^\alpha\cos(\pi\alpha)+1]^{(D+\lambda)/4\alpha}}dy. \qquad (13)$$

Figure 2 shows the velocity distribution corresponding to the GML energy distribution with $D = 3$ and $\lambda = 1/3$. Distributions with several values of α are plotted. With $\alpha = 1$, the distribution is reduced to a Gaussian. With $\alpha \lesssim 1$, the distribution has a similar profile to a Gaussian around the central region, although it has bigger wings. With a smaller value of α (with larger energy dissipation), the wing intensity becomes bigger.

In Fig. 2(b), the same profiles are shown in a log-log plot. As expected from the energy distribution Fig. 1, the velocity distribution also has a power-law tail. The dotted lines in the figure show the power-law dependence $\propto |v|^{-2\alpha-\lambda-1}$.

III. DIRECT MOLECULAR DYNAMICS SIMULATION

The previous discussion focuses on energy dissipation and relaxation [Eq. (4)] and assumes that the energy source is at the high-energy limit. However, in realistic situations, there should be an energy cutoff at the energy scale of the heat source, and thus the power-law tail in Fig. 2 only lasts up to this energy scale. In order to see the validity of the previous discussion, as well as the effect of the energy cutoff, in this section a comparison is made to some simple numerical simulations.

In Sec. III A, a comparison is carried out for inelastic particles systems, which has been considered in the original work [14–16]. More relevant simulation of the radical atoms in plasmas is carried out by direct molecular dynamics simulations in Sec. III B.

A. Heated inelastic particles

Similarly to Ref. [14,15], Monte Carlo simulations for a spatially uniform ensemble of inelastic particles are carried out. At every step of the simulation, we randomly choose the colliding pairs of particles and compute their scattering and energy dissipation based on relative velocity of the two particles and the collision geometry. The two particles experience inelastic collisions, where the relative velocity along the collision normal is reduced by the factor of $1 - r$ with elasticity r [25,26]. As an energy injection process, we choose a particle randomly at a certain rate and replace their velocity with Maxwellian with temperature 1. The energy injection rate is kept constant and the simulation is continued until the system reaches a steady state.

Figure 3(a) shows the simulated steady-state energy distribution for inelastic particles in a three-dimensional space ($D = 3$) with the Maxwell interaction ($\lambda = 0$), which is discussed in Sec. II A. Simulation results with different values of r are plotted with appropriate offsets. The distribution with $r = 1$ (elastic limit, with no heating) falls exponentially in the high-energy region, while with $r < 1$ the distribution has a power-law tail. Bigger tails are seen in the distribution with larger energy dissipation, i.e., the smaller values of r.

In order to see the validity of the above theory, the GML distribution [Eqs. (7) and (8)] is fitted to the simulated energy distribution. The bold curves in Fig. 3(a) show the best fit by the GML distribution, where two parameters, the energy scale $\langle E\rangle_\alpha$ and the stability parameter α, are adjusted. The GML distribution well represents the simulated energy distributions, particularly those under the small dissipation.

Ben-Naim *et al.* have reported an analytical representation of the power-law index of the velocity distribution at the high-velocity region. They consider the high-velocity limit where the velocity distribution is approximated by $f(v) \propto v^{-\sigma}$ and derive the representation of σ as a function of the inelasticity r, the spatial dimension D, and the interparticle interaction λ [14,15],

$$\frac{1-{}_2F_1\left(\frac{D+\lambda-\sigma}{2},\frac{\lambda+1}{2},\frac{D+\lambda}{2},1-r^2\right)}{(1-r)^{\sigma-D-\lambda}} = \frac{\Gamma\left(\frac{\sigma-D+1}{2}\right)\Gamma\left(\frac{D+\lambda}{2}\right)}{\Gamma\left(\frac{\sigma}{2}\right)\Gamma\left(\frac{\lambda+1}{2}\right)}, \qquad (14)$$

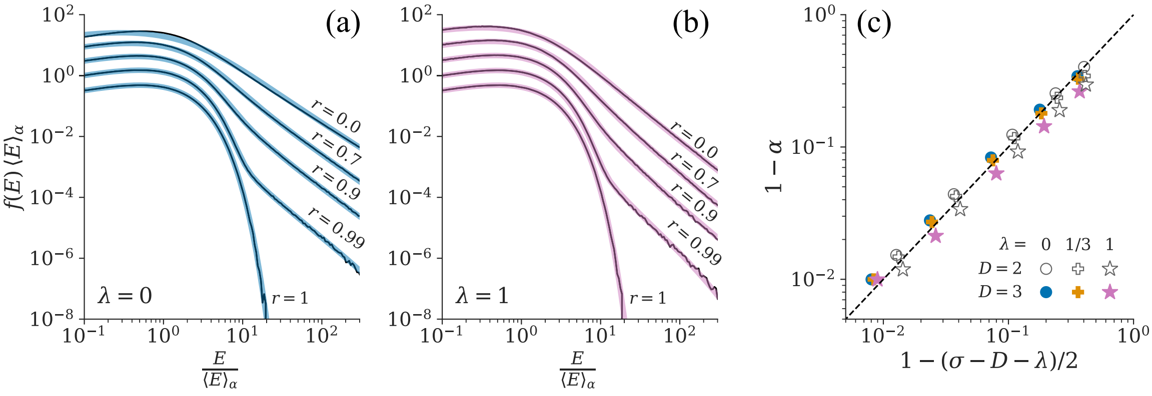

FIG. 3. Steady-state distributions of isotropic inelastic gases by the Monte Carlo simulations. Thin curves: The simulation results for (a) the gases with Maxwell interaction and (b) for the hard spheres. Results with several values of the inelasticity r are shown, with an appropriate vertical offset for the sake of clarity. Thick curves: The best fit by the GML distribution. (c) Comparison between the optimum values of α evaluated from the simulated energy distribution and the theoretical values of the power-law index, Eq. (14).

where ${}_2F_1$ is the hypergeometric function. The power-law index for the energy distribution is written by $(\sigma - D)/2 + 1$. On the other hand, the power-law index of the high-energy tail of the GML distribution can be written by $\alpha + \lambda/2 + 1$.

Figure 3(c) compares the best-fit values of α and the theoretical predictions of σ [Eq. (14)]. As the GML-fit mainly accounts for the tail intensity (recall that the tail behaves $f(E) \approx E^{-\alpha-1}/[(\langle E\rangle_\alpha)^\alpha \Gamma(1-\alpha)]$, rather than the power-law index of the tail, a good agreement in Fig. 3(c) indicates the consistency of our discussion to the previous works. Note that the statistical uncertainty in the value of α is small compared with the marker size.

Similar Monte Carlo simulations have been carried out also for inelastic particles with the hard-sphere interaction, $\lambda = 1$. The steady-state solutions for several values of r are shown in Fig. 3(b). The bold curves show the best fit by the modified GML distribution, Eq. (11). This well approximates the simulated energy distributions, as well. The best-fit α is plotted in Fig. 3(c), with more simulations with $\lambda = 1/3$ and $D = 2$. They are again consistent with Eq. (14), suggesting the validity of GML distribution for this system.

B. Heated atoms surrounded by cold walls

In the previous simulation, the collided particles immediately forget the previous collision and the next particle to be collided is chosen randomly from the ensemble, i.e., the correlation effect is not considered. In this subsection, a more realistic simulation including the correlation effect is presented. The system considered here is as follows (also illustrated in Fig. 4):

(1) (Energy randomization) N atoms with mass m are in a cubic box with one side of L. These atoms interact according to the interatomic potential $V(R) = (R/R_0)^{-6}$, where R is the interatomic distance and R_0 is the spatial scale.

(2) (Energy dissipation) The walls have infinitely large degrees-of-freedom and have much lower temperatures than the atomic gas. A collision with the walls is approximated by an inelastic collision [27], where the atomic velocity perpendicular to the wall changes $v_\perp \to -rv_\perp$ with the inelastic coefficient of the walls r. $r = 1$ indicates elastic collisions.

(3) (Heating) The box has an opening with the area of a. If an atom goes out of the box through this opening, then another atom having the temperature T_0 is injected into the box.

In a steady state, this energy injection will be balanced with the energy dissipation by the wall collisions.

The steady-state velocity distribution of the atoms in this system is simulated with a molecular-dynamics simulator `lammps` [28]. Used are $m = 1$, $L = 1$, $a = 10^{-3}$, $R_0 = 10^{-3}$, $T_0 = 1$, and the time step of 2×10^{-5} for all the simulation results. The values of r and N are scanned for later comparison. The simulation is continued until the system reaches the steady state.

Figure 5 shows the steady-state velocity distribution for $r = 0.99$ and $N = 3 \times 10^3$. The simulated velocity distribution has slowly decaying wings in high-velocity regions. For a comparison, the best-fit Gaussian distribution is shown by a thin gray curve. Figure 5(b) shows the same figure in a log-log plot. It can be seen that the velocity distribution has a power-law tail in the high-velocity region up to $|v| \approx 2$, which roughly corresponds to the velocity scale of the heat source.

The bold curve in Fig. 5 shows the best fit by GML velocity distribution. Here $\lambda = 1/3$ is used based on the Van der Waals interparticle potential used in the simulation. The GML

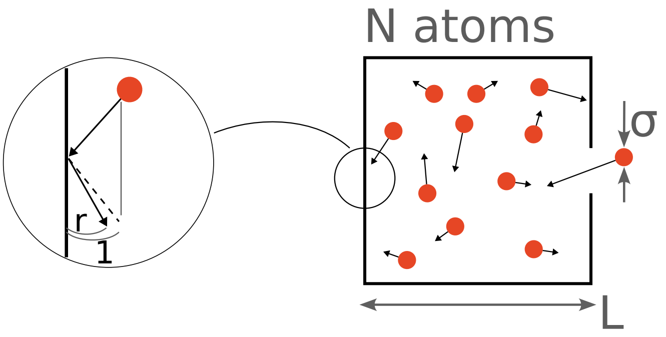

FIG. 4. A schematic illustration of our direct molecular dynamics simulation. N atoms are confined by a cold box, where atoms will lose their kinetic energy by wall collisions. The box has a small opening and once an atom leaves the box through this opening, a high-energy atom with temperature T_0 is injected.

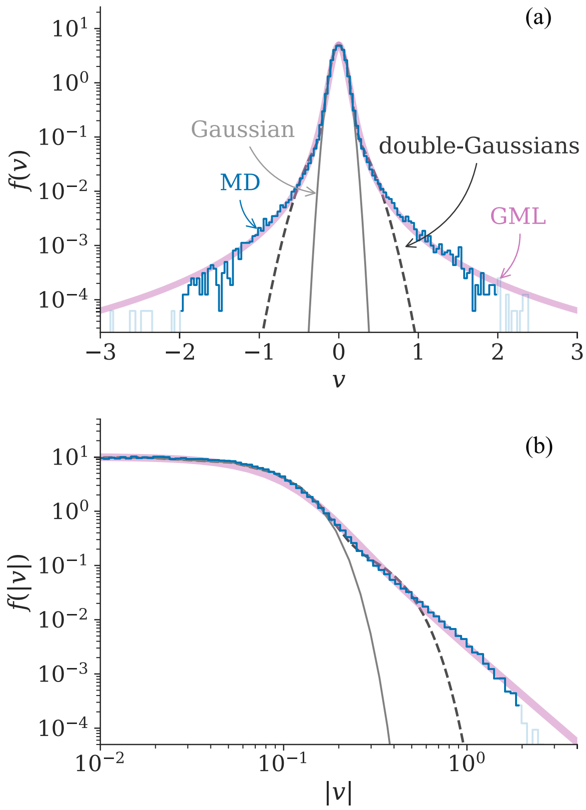

FIG. 5. MD: The steady-state velocity distribution in the system shown in Fig. 4 by the direct molecular dynamics simulation. $N = 3 \times 10^3$ and $r = 0.99$ is used. Panels (a) and (b) show the same distribution but in a semilog plot and log-log plot, respectively. The thin solid curve shows the best fit by a Gaussian function. The simulated velocity distribution has a similar shape to a Gaussian around the low-velocity region, while in the high-velocity region it has a power-law dependence. The velocity of the heat source is ≈ 2, forming a cutoff of the power-law dependence. The bold curve shows the best fit by the GML velocity distribution Eq. (13). The thin dashed curve shows the best fit by the double-Gauss function.

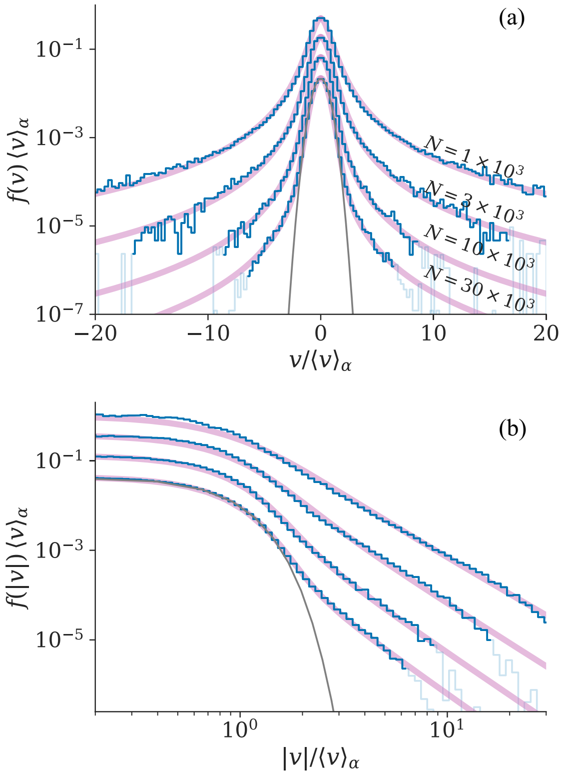

FIG. 6. Simulated steady-state velocity distributions with different values of N. The horizontal axis is normalized by the velocity scale $\langle v\rangle_\alpha$, while in the vertical direction an appropriate offset is introduced for the sake of clarity. The intensity of the power-law tail is smaller to the larger-N simulation because of more significant entropy production by elastic collisions among particles. The bold curves show the best fit by the GML velocity distribution. The GML velocity distribution well captures the velocity distribution for all the conditions, particularly with large-N systems.

distribution well captures the simulated velocity distribution, both the central and wing region, up to the velocity cutoff by the heat source. Here the number of adjustable parameters is two, which are the energy scale and α. The optimum value of α at the best fit is 0.903 ± 0.002 for this case.

As a reference, the best fit by a double-Gauss function is shown by a dotted curve. Although the number of adjustable parameters for the double-Gauss fit (three, two energy scales and the intensity ratio of the two Gaussians) is more than that in the GML fit, the double-Gaussian fails to represent the wings with the power-law decay.

Similar simulations are carried out with different values of N. The simulated velocity distributions are shown in Fig. 6. Note that the horizontal axis is the velocity normalized by $\langle v\rangle_\alpha \equiv \sqrt{2\langle E\rangle_\alpha/m}$ for clearer presentation of the shape difference. Here $\langle E\rangle_\alpha$ is obtained by the GML fit, which is described later. With a larger number of particles in the box N, the profile becomes closer to a Gaussian distribution and the wing intensity becomes smaller. This is consistent with the larger rate for the entropy production by elastic collisions. The best-fit GML velocity distribution is shown by bold curves. The GML velocity distribution well captures the simulated velocity distribution. The quality of the fit is better at the smaller dissipation condition. This is consistent because the approximation Eq. (7) is derived with $\Delta \ll 1$. Figure 7 shows the N dependence of the best-fit value of α, as functions of N and r.

The theoretical relation between α and other quantities may be derived from Eq. (6). With the diffuse collision kernel Eq. (2), Eq. (6) can be reduced to

$$1 = (1-\xi)\frac{B\left(\frac{D}{2}+\alpha, \frac{D}{2}\right)}{B\left(\frac{D}{2}, \frac{D}{2}\right)} + \xi e^{-\Delta}. \tag{15}$$

By assuming that $\Delta \ll 1$ and $1-\alpha \ll 1$,

$$1-\alpha \approx \frac{\xi}{1-\xi}\Delta\left\{\psi(D) - \psi\left(\frac{D}{2}\right) - \frac{1}{D}\right\}, \tag{16}$$

can be obtained, where $\psi(z) \equiv \Gamma(z)'/\Gamma(z)$ is the digamma function. For our particular system, $\Delta \approx (1-r^2)/D$. Here $\xi/(1-\xi)$ is the frequency ratio between elastic and wall collisions. The collision frequency of the elastic collisions is $\sqrt{2}\langle v\rangle_\alpha \sigma N/L^3$, where the viscosity cross section at the energy

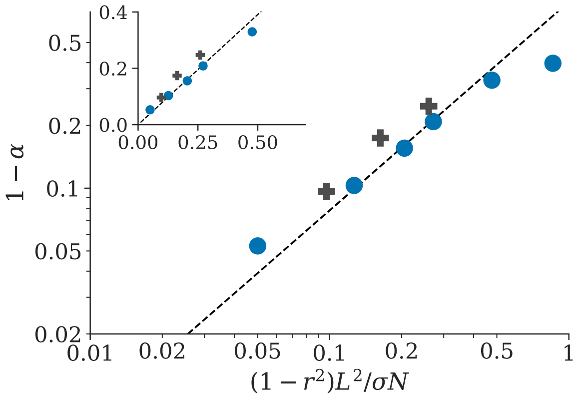

FIG. 7. N and r dependence of the best-fit α. The circles and crosses indicate the simulation results with $r = 0.99$ and 0.95, respectively. The results are consistent with the theoretical prediction (dotted diagonal line), particularly with a small dissipation condition. The inset shows the same relation but with a linear scale.

of $2\langle E\rangle_\alpha$ is used for $\sigma \approx \pi R_0^2(2\langle E\rangle_\alpha)^{1/3}$ [29]. The collision frequency with the surrounding six walls is $\approx 6\langle v\rangle_\alpha/L$. From these numbers and $D = 3$, we obtain

$$1 - \alpha \approx 0.78(1 - r^2)\frac{L^2}{\sigma N}. \tag{17}$$

The dotted diagonal line in Fig. 7 shows Eq. (17). The simulated results with $r = 0.99$ and 0.95 for several values of N are close to this diagonal line. This shows a reasonable agreement with our theory, despite the significant simplification.

IV. EXPERIMENTAL OBSERVATIONS

In this section, the GML distribution is compared with experimentally observed velocity distributions of atoms in plasmas. The theory shown above is applicable when

(i) a system has a particle source at the high-energy region,

(ii) particles in the system experience elastic collisions and wall collisions,

(iii) the wall temperature is much smaller than the energy of the particle source,

(iv) the rate of wall collision is similar to or less than the elastic-collision rate.

This applies particularly to radical atoms in plasmas, because of the natural heating mechanism through molecular dissociation. For example, the scale of the Franck-Condon energy gained by a hydrogen atom dissociated from a hydrogen molecule is 2 eV [7–9], which is much larger than the wall temperature (typically 0.05 eV). Also, a large elastic-collision cross section among radical atoms through Van der Waals interaction contributes to the applicability of the theory, although caution should be always exercised whether the system is collisional enough.

In order to observe the universality of the GML velocity distribution, it is compared with several experimental observations. In Secs. IV A and IV B, the velocity distributions of hydrogen atoms and oxygen atoms are analyzed, which have been observed with laser-based methods (Refs. [30] and [6], respectively) and reported in the literature. In their original publications, these distributions have been analyzed by a two-temperature Maxwellian. It is shown here that the GML distribution also well represents the observations. This suggests the universality of the collisional-energy-cascade in plasmas. In Sec. IV C, unreported high-resolution emission spectra of neutral carbon and oxygen atoms found in a public data archive [31] are studied.

A. Hydrogen atom velocity distribution measured by laser-induced-fluorescence spectroscopy

Amorim *et al.* have directly measured the velocity distribution of ground-state hydrogen atoms in a microwave discharge tube with a hydrogen–nitrogen mixture [2,30]. They inject frequency-tripled 615-nm laser (205-nm photon) into the plasma and the ground-state hydrogen atoms in the plasma are excited by two-photon absorption ($1s\ ^2\mathrm{S} \rightarrow 3d\ ^2\mathrm{D}$). They observe the subsequent fluorescence ($3d\ ^2\mathrm{D} \rightarrow 2p\ ^2\mathrm{P}$, 656-nm transition). From the fluorescence intensity as a function of the laser wavelength, the velocity distribution of the ground-state hydrogen atoms is obtained. Their 615-nm laser has 0.08 cm^{-1} (0.03 nm) linewidth. The linewidth of the frequency tripled 205-nm laser is not given in the original paper and is not straightforward to estimate as this involves the nonlinear conversion, but this might correspond to $\approx 10^0$ km/s in speed. The data points are extracted from their electronic manuscript, where the data are embedded in an `xml` format, which is shown by markers in Fig. 8. The horizontal axis is the velocity along the sight line, converted from $v = c\Delta\lambda/\lambda_0$, where c is the light speed, $\Delta\lambda$ is the wavelength displacement, and λ_0 is the line center. The thin solid curve in Fig. 8 is the best fit by a Gaussian function. The central part of the velocity distribution is close to a Gaussian distribution, while it has much larger wings. The wings profile is similar to a power-law dependence.

In their system, the energetic hydrogen atoms have been attributed to the photo-dissociation of ammonia [30]. These energetic atoms may distribute their energy to other particles by elastic collision. The injected energy should be eventually dissipated probably to the chamber walls; otherwise, the atom temperature will increase up to the injection temperature in a steady state. Therefore, their experimental condition is similar to that considered in this work: The existence of the energy injection at the high-speed region, energy dissipation, and elastic collisions among particles.

The bold curve in the figure shows the best fit by the GML velocity distribution. The GML velocity distribution well captures the observation, the Gaussian-like central part as well as the power-law decay in the tail, up to the energy cutoff around $|v| \approx 10^4$ m/s. The optimum value of α obtained by the fit is 0.58. Note that a small discrepancy in the low-speed region may be caused not only by the approximation introduced in Eq. (7) but also by the finite resolution of the measurement ($\approx 10^0$ km/s).

From the optimum value of α and Fig. 7, we obtain $(1 - r^2)L^2/\sigma N \approx 1$. From the chamber diameter $L \approx 0.016$ m, the elastic collision cross section among hydrogen atoms $\sigma \approx 3 \times 10^{-19}\ \mathrm{m}^2$ [32], and the expected atom density in the plasma $NL^{-3} \approx 10^{19}\ \mathrm{m}^{-3}$ [30]; the value of r is estimated as ≈ 0.98. This is in a reasonable order for the inelasticity of a solid surface [27]. As the reflection coefficient is one of the

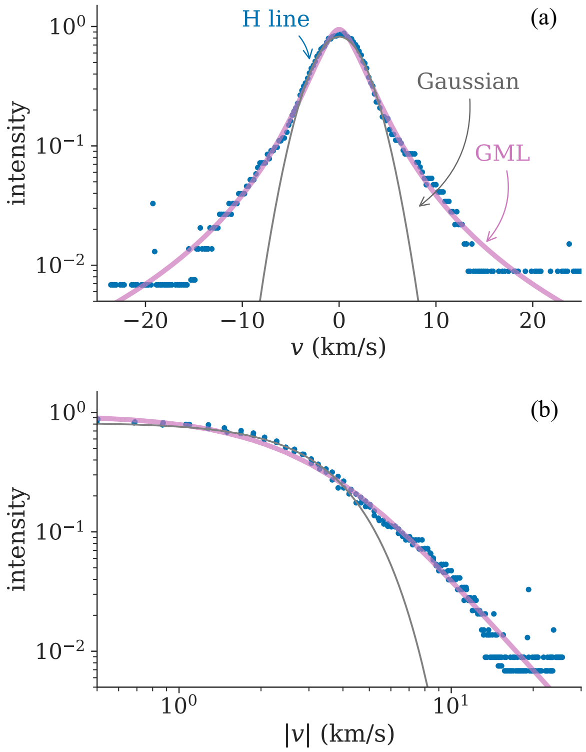

FIG. 8. The velocity distribution of hydrogen atoms in hydrogen–nitrogen mixture plasma observed by Amorim *et al.* [2,30]. The thin curve indicates the best-fit Gaussian, while the bold curve is the best-fit GML velocity distribution. The optimum value of α is 0.58. The high-velocity tail is well captured by the GML velocity distribution. The small discrepancy in the low-speed region may be due to the measurement resolution, which is $\approx 10^0$ km/s. Panel (b) is the same data for (a) but in a log-log plot.

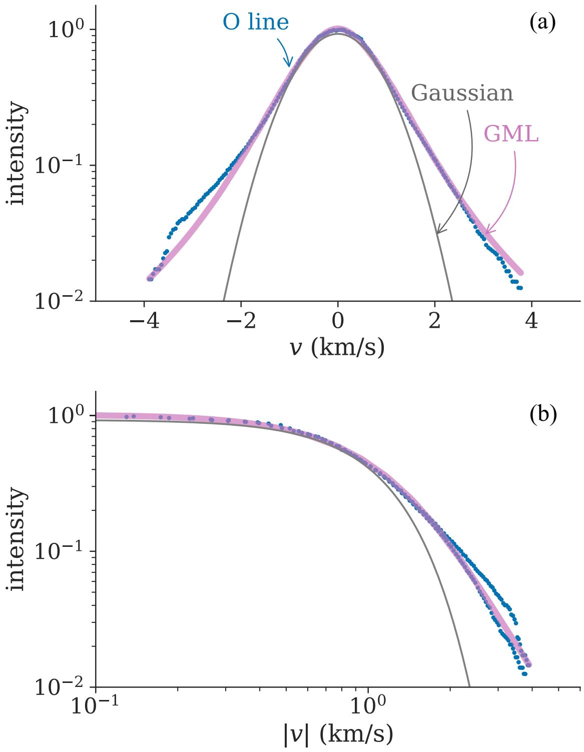

FIG. 9. The velocity distribution of oxygen atoms in helicon-wave-heated plasma of oxygen, observed with absorption spectroscopy based on a semiconductor-diode laser, reported by Sasaki *et al.* [6]. The thin curve indicates the best-fit Gaussian, while the bold curve is the best-fit GML velocity distribution. The optimum value of α is 0.73. The central part and the high-velocity tails are well captured by the GML velocity distribution. The discrepancy in the far wings is attributed to the error in the zero level in the absorption spectrum.

difficult quantities to measure *in situ*, the use of the GML distribution may provide a possibility to estimate only from the spectrum, although in this rough estimate we ignored the collision with other species, such as collisions with hydrogen molecules.

B. Oxygen atom velocity distribution measured by laser absorption spectroscopy

Sasaki *et al.* have measured the velocity distribution of metastable-state oxygen atoms in a helicon-wave heated plasma of oxygen [6]. The back-filled gas pressure and the helicon-wave power in their experiment shown here are 30 mTorr and 1.5 kW, respectively. They inject a semiconductor-diode laser at 777.5 nm into the plasma and observe the absorption by the metastable oxygen transition $2s^2 2p^3 (^4\mathrm{S}^\mathrm{o}) 3s\ ^5\mathrm{S}_2^\mathrm{o} \rightarrow 2s^2 2p^3 (^4\mathrm{S}^\mathrm{o}) 3p\ ^5\mathrm{P}_1$. By scanning the laser frequency, the absorption spectral profile (in this case the Doppler broadening is dominant) is obtained.

Figure 9 shows the velocity distribution of oxygen atoms, which is extracted from their electronic manuscript. The horizontal axis is the velocity along the sight line, converted from $v = c\Delta\lambda/\lambda_0$ where $\lambda_0 = 777.5$ nm is the line center. As the linewidth of the diode laser is much smaller than the Doppler width of oxygen at room temperature, the effect of the instrumental profile is virtually negligible. On the other hand, an accurate intensity measurement at the far wings is more difficult to obtain in absorption spectroscopy.

The thin solid curve in Fig. 8 is the best fit by a Gaussian function. The central part of the velocity distribution is close to a Gaussian distribution, while it has much larger wings. In their system, it has been suggested that the energetic oxygen atoms have been attributed to electron-impact dissociation of oxygen molecules [6], similarly to the hydrogen atoms discussed in the previous subsection. Originally, this nonthermal velocity distribution has been analyzed by a two-temperature Maxwellian.

The bold curve in the figure shows the best fit by the GML velocity distribution. The GML velocity distribution well captures the observation. The optimum value of α obtained by the fit is 0.73 ± 0.01. From the optimum value of α and Fig. 7, we obtain $(1 - r^2)L^2/\sigma N \approx 0.3$. Their chamber diameter is $L \approx 0.016$ m, and the oxygen density in the plasma is estimated from the back-fill pressure 30 mTorr and the dissociation ratio and energy scale $\approx$1000 K to be $NL^{-3} \approx 3 \times 10^{20}$ m^{-3}. From the elastic collision cross section among oxygen atoms $\sigma \approx 2 \times 10^{-19}$ m^2 [33], the value of r is estimated as $\approx$0.84.

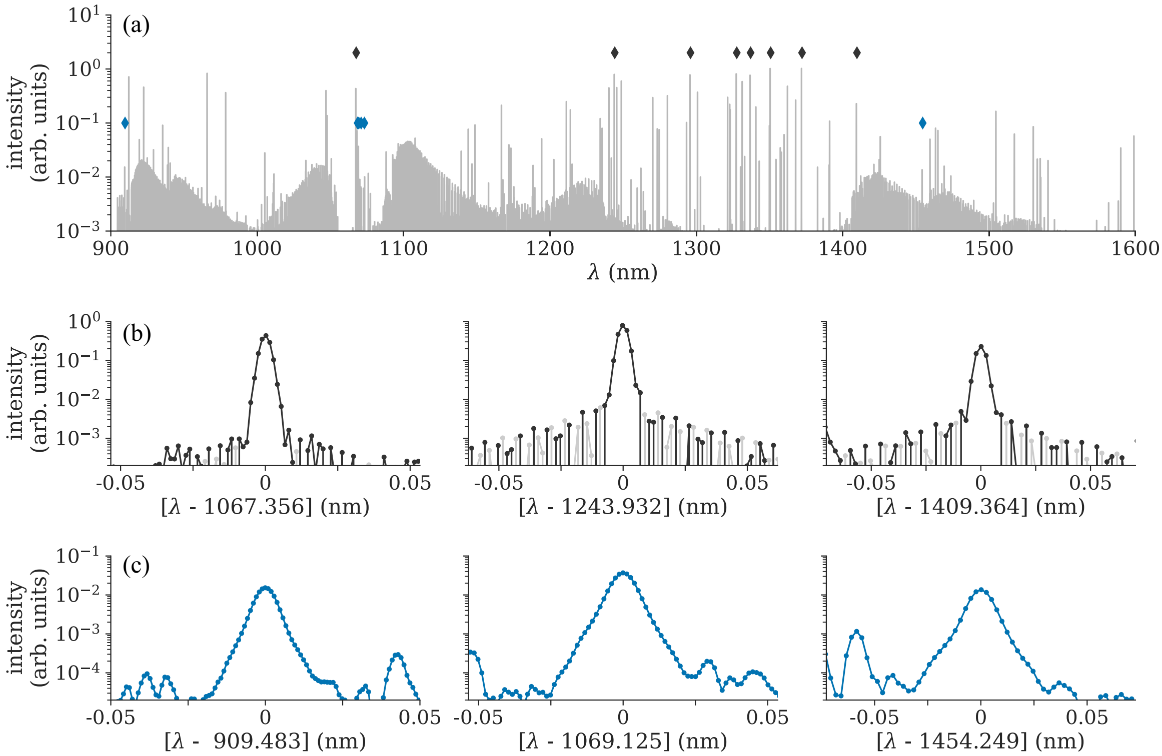

FIG. 10. (a) Spectrum observed in NSO [31]. Gray and blue markers show the wavelengths of the argon and carbon lines, respectively, shown in Fig. 11. (b) Expanded spectra of three argon lines. The light gray markers show the negative points (multiplied by -1), representing the oscillation of the instrumental side robes. (c) Expanded spectra of three carbon lines.

This is again in a reasonable order for the inelasticity of a solid surface [27].

C. Carbon and oxygen atom velocity distributions measured by emission spectroscopy

As a third example, consider a high-resolution spectrum measured at the National Solar Observatory, the electronic data of which are obtained from its historical data archive (file name `770612R0.010` [31]). This spectrum was originally measured to study the cyanide spectra in 1977 from a microwave discharge with a mixture of carbon, nitrogen, and argon, with a high-resolution Fourier transform spectrometer with a 1-m optical path difference in the wavelength range $\lambda = 830$–2710 nm. The wavelength resolution is 3.5 pm (as the full width half maximum) for this measurement. Figure 10(a) shows the original data and Figs. 10(b) and 10(c) show expanded views for argon lines at $\lambda = 1067.36$ nm $(3s^23p^5(^2\mathrm{P}^{\mathrm{o}}_{3/2})4p\ ^2[1/2]_1 \leftarrow 3s^23p^5(^2\mathrm{P}^{\mathrm{o}}_{3/2})5s\ ^2[3/2]^{\mathrm{o}}_2)$, 1243.93 nm $(3s^23p^5(^2\mathrm{P}^{\mathrm{o}}_{3/2})4p\ ^2[1/2]_1 \leftarrow 3s^23p^5(^2\mathrm{P}^{\mathrm{o}}_{3/2})3d\ ^2[3/2]^{\mathrm{o}}_2)$, and 1409.36 nm $(3s^23p^5(^2\mathrm{P}^{\mathrm{o}}_{3/2})4p\ ^2[1/2]_0 \leftarrow 3s^23p^5(^2\mathrm{P}^{\mathrm{o}}_{3/2})3d\ ^2[3/2]^{\mathrm{o}}_1)$, and carbon lines at $\lambda = 909.48$ nm $(2s^22p3s\ ^3\mathrm{P}^{\mathrm{o}}_2 \leftarrow 2s^22p3p\ ^3\mathrm{P}_2)$, 1069.125 nm $(2s^22p3s\ ^3\mathrm{P}^{\mathrm{o}}_2 \leftarrow 2s^22p3p\ ^3\mathrm{D}_3)$, and 1454.25 nm $(2s^22p3s\ ^1\mathrm{P}^{\mathrm{o}}_1 \leftarrow 2s^22p3p\ ^1\mathrm{P}_1)$, respectively.

The observed linewidth of the argon lines is 5.2 pm. This is consistent with the convolution of the argon Doppler width at room temperature (3.7 pm) and the instrumental width. The oscillation seen in the argon line wings, i.e., the side robe, originates from the instrumental function of this spectrometer. Since this spectrometer is based on Fourier transform principles, the spectrum is affected by the window function, such as the sinc function $\frac{\sin(\pi\Delta\lambda/\delta_\lambda)}{\pi\Delta\lambda/\delta_\lambda}$ for a rectangular window, where δ_λ is the spectral resolution. Although other line broadenings, such as Doppler broadening, average out this oscillation in the instrumental side robes, this is still apparent in the argon lines because of their similar Doppler widths to the instrumental width. This effect is negligible for the carbon lines owing to their larger Doppler widths.

Figure 11 shows all the emission lines of neutral carbon atoms in the wavelength range 900–1600 nm that are intense enough and isolated from other lines, i.e., 909.48 nm $(2s^22p3s\ ^3\mathrm{P}^{\mathrm{o}}_2 \leftarrow 2s^22p3p\ ^3\mathrm{P}_2)$, 1068.31 nm $(2s^22p3s\ ^3\mathrm{P}^{\mathrm{o}}_1 \leftarrow 2s^22p3p\ ^3\mathrm{D}_2)$, 1068.54 nm $(2s^22p3s\ ^3\mathrm{P}^{\mathrm{o}}_0 \leftarrow 2s^22p3p\ ^3\mathrm{D}_1)$, 1069.12 nm $(2s^22p3s\ ^3\mathrm{P}^{\mathrm{o}}_2 \leftarrow 2s^22p3p\ ^3\mathrm{D}_3)$, 1070.73 nm $(2s^22p3s\ ^3\mathrm{P}^{\mathrm{o}}_1 \leftarrow 2s^22p3p\ ^3\mathrm{D}_1)$, 1072.95 nm $(2s^22p3s\ ^3\mathrm{P}^{\mathrm{o}}_2 \leftarrow 2s^22p3p\ ^3\mathrm{D}_2)$, and 1454.25 nm $(2s^22p3s\ ^1\mathrm{P}^{\mathrm{o}}_1 \leftarrow 2s^22p3p\ ^1\mathrm{P}_1)$. They are plotted as functions of the velocity along the sight line, converted by $v = c\Delta\lambda/\lambda_0$, and with their areas normalized. All the emission lines have the same profile. Since the Stark broadening and the pressure broadening have different sensitivities depending on the transition, these effects may be negligible. From the neutral argon emission lines observed at the same time (gray points in Fig. 11), it is found that the instrumental broadening is also negligible on the carbon line profiles. It is reasonable to assume that the Doppler broadening is dominant that reflects the velocity distribution of ground-state neutral carbon atoms.

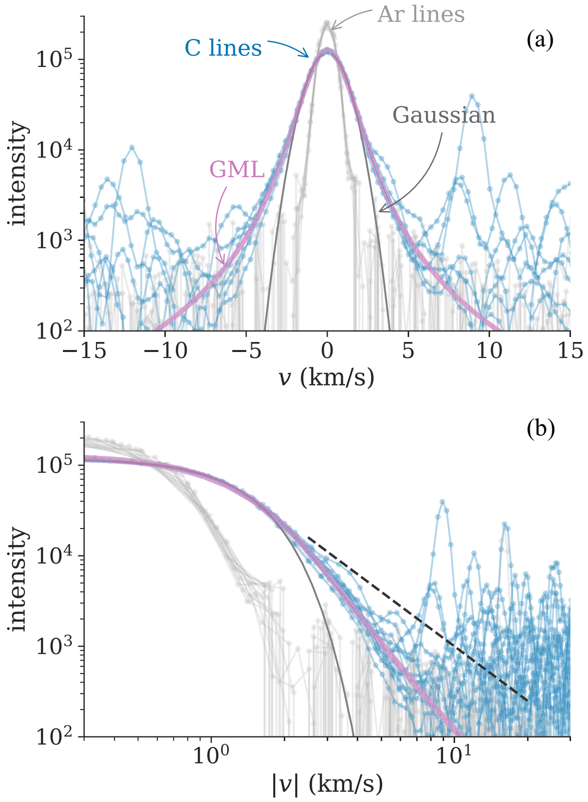

FIG. 11. Emission spectra of neutral carbon atoms measured for carbon-nitrogen-argon plasma at the National Solar Observatory [31]. $\lambda_0 = 909.48$-, 1068.31-, 1068.54-, 1069.12-, 1070.73-, 1072.95-, and 1454.25-nm lines are plotted with the area normalized to unity. The thin and bold curves show the best fit by the Gaussian and the GML velocity distribution, respectively. The Lorentzian decay $|v|^{-2}$ is shown by a dotted line, which is much slower than the experimental decay. Eight neutral argon emission spectra ($\lambda_0 =$ 1243.93, 1295.67, 1327.26, 1331.32, 1336.71, 1350.42, 1362.27, and 1371.86 nm) are also shown by gray points, which indicate the negligible effect of the instrumental profile on the carbon profiles.

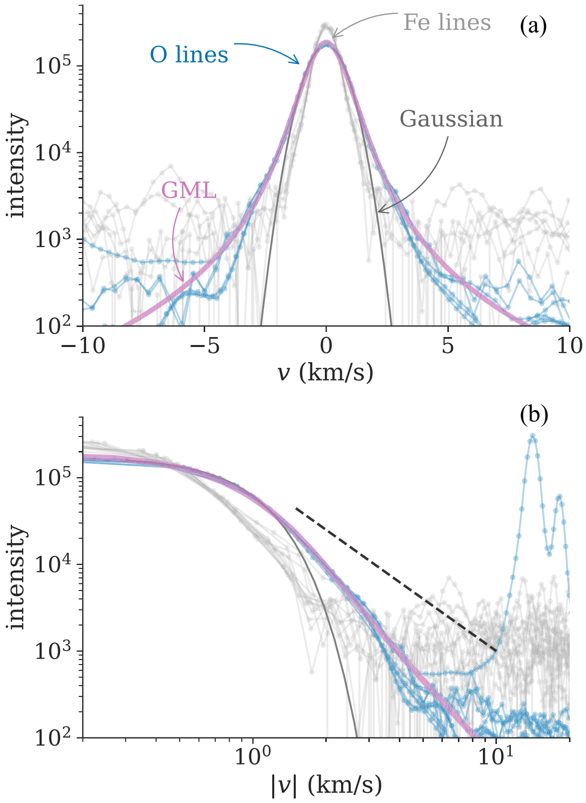

FIG. 12. Emission spectra of neutral oxygen atoms measured for iron–helium–carbon monoxide mixture plasma at the National Solar Observatory [31]. $\lambda_0 = 777.19$-, 777.42-, 777.54-, 844.68-, 1129.77-, and 1130.24-nm lines are plotted with the area normalized to unity. The thin and bold curves show the best fit by the Gaussian and the GML velocity distribution, respectively. The Lorentzian decay $|v|^{-2}$ is shown by a dotted line, which is much slower than the experimental decay. Seven neutral iron emission spectra ($\lambda_0 =$ 744.58, 758.60, 793.71, 794.58, 851.41, 886.69, and 973.86 nm) are also shown by gray points, which indicate the negligible effect of the instrumental profile on the oxygen profiles.

The best fit by a single Gaussian to the carbon lines is shown by a thin curve in Fig. 11. The carbon profile shows significant tails compared with a Gaussian function, indicating a strong nonthermality of their velocity distribution. In a log-log plot [Fig. 11(c)], the velocity distribution is close to a power-law in a large-$|v|$ region.

Carbon atoms in plasmas may also experience heating due to molecular dissociation, entropy production through elastic collision, and energy dissipation by the wall collision. The GML velocity distribution may be a good candidate to describe this nonthermal velocity distribution. The bold curve shows the best fit by the GML velocity distribution. The entire profile is well represented by this function and from the fit $\alpha = 0.78 \pm 0.01$ is obtained.

As this spectrum has a good signal-to-noise ratio, the difference from a Lorentz profile can be also clearly seen. The Lorentz profile arises when the upper or lower quantum states are perturbed, for example, by the simultaneous emission (natural broadening), electron impact (Stark broadening), or neutral atom impact (pressure broadening). The convolution of the Lorentz profile and Gaussian profile (thermal motion or instrumental broadening) gives the Voigt profile. One of the important properties of both Lorentz and Voigt profiles is the wing decay, i.e., $\propto |\Delta\lambda|^{-2}$, where $\Delta\lambda$ is the wavelength shift from the line center. This contrasts with the GML distribution with the Van der Waals interaction, which decays $\propto |\Delta\lambda|^{-2\alpha-4/3}$. The dotted line in Fig. 11 shows the Lorentzian decay $\propto |\Delta\lambda|^{-2}$, which is inconsistent with the experimental profile.

A similar spectrum for oxygen atoms can be also found in the same data archive (file `801015R0.100` in Ref. [31]). Figure 12 shows the same plot but for an iron–helium–carbon monoxide mixture plasma. Blue points represent the emission line profiles from neutral oxygen, 777.19 nm ($2s^2 2p^3 (^4\mathrm{S}^\mathrm{o}) 3s\ ^5\mathrm{S}^\mathrm{o}_2 \leftarrow 2s^2 2p^3 (^4\mathrm{S}^\mathrm{o}) 3p\ ^5\mathrm{P}_3$), 777.42 nm ($2s^2 2p^3 (^4\mathrm{S}^\mathrm{o}) 3s\ ^5\mathrm{S}^\mathrm{o}_2 \leftarrow 2s^2 2p^3 (^4\mathrm{S}^\mathrm{o}) 3p\ ^5\mathrm{P}_2$), 777.54 nm ($2s^2 2p^3 (^4\mathrm{S}^\mathrm{o}) 3s\ ^5\mathrm{S}^\mathrm{o}_2 \leftarrow 2s^2 2p^3 (^4\mathrm{S}^\mathrm{o}) 3p\ ^5\mathrm{P}_1$), 844.68 nm ($2s^2 2p^3 (^4\mathrm{S}^\mathrm{o}) 3s\ ^3\mathrm{S}^\mathrm{o}_1 \leftarrow 2s^2 2p^3 (^4\mathrm{S}^\mathrm{o}) 3p\ ^3\mathrm{P}_1$), 1129.77 nm ($2s^2 2p^3 (^4\mathrm{S}^\mathrm{o}) 3p\ ^5\mathrm{P}_2 \leftarrow 2s^2 2p^3 (^4\mathrm{S}^\mathrm{o}) 4s\ ^5\mathrm{S}^\mathrm{o}_2$), and 1130.24 nm ($2s^2 2p^3 (^4\mathrm{S}^\mathrm{o}) 3p\ ^5\mathrm{P}_3 \leftarrow 2s^2 2p^3 (^4\mathrm{S}^\mathrm{o}) 4s\ ^5\mathrm{S}^\mathrm{o}_2$). They are plotted as functions of the velocity along the sight line and with their area normalized unity. All the profiles show a similar distribution. Also, the comparison with neutral iron lines (744.58, 758.60, 793.71, 794.58, 851.41, 886.69, and 973.86 nm) shown by gray points in Fig. 12 indicates the negligible effect by the instrumental broadening. Similarly to the previous discussion, this suggests that the Doppler effect is the dominant broadening mechanism for these lines.

The thin solid curve shows the best-fit Gaussian to these profiles. The observed neutral oxygen spectra show significant wing intensity than the Gaussian. In a log-log plot, it is close to a power-law distribution. The bold curves in Fig. 12 show the best fit by the GML velocity distribution. The entire profile is well represented by this function, with $\alpha = 0.77 \pm 0.01$ from the fit.

V. SUMMARY AND DISCUSSIONS

In this work, an application of the collisional-energy-cascade model to the nonthermal velocity distribution of radical atoms in plasmas has been proposed, which consists of a heat source at the high-energy limit, entropy production by elastic collisions, and energy dissipation. The GML distribution is shown to represent a steady-state velocity distribution for this model.

This model is compared with a direct molecular dynamics simulation. The simulated velocity distribution is well represented by the GML distribution. Furthermore, the stability parameter in the GML distribution, which indicates the fractional importance of the entropy production against the energy dissipation, is consistent with the theoretical prediction.

The Doppler profiles spectroscopically observed for neutral radical atoms in plasmas are also compared with this model. They have much stronger wing intensities than a Gaussian function, similar to the molecular dynamics simulation. The GML velocity distribution well represents the observed velocity distributions, indicating that the collisional energy cascade is universally seen in plasmas.

Historically, nonthermal velocity distributions have been analyzed by two-temperature Maxwellians. One of the advantages of the GML distribution is that this distribution is based on kinetic theory. The physical knowledge of the system, particularly the stability parameter representing the degree of nonthermality, can be obtained by fitting the GML distribution to the observed spectrum. Furthermore, as the GML distribution has fewer adjustable parameters (the velocity scale and the stability parameter) than the two-temperature Maxwellian (two velocity scales and the fractions of the two Maxwellians), the GML distribution is more robust. The GML distribution may provide a new spectroscopy tool to analyze spectra showing nonthermal Doppler profiles.

Despite strong support by kinetic theory, the GML distribution has some limitations. The two-temperature model uses Gaussians, which are favorable when taking instrumental broadening into account, as the convolution of two Gaussians becomes another Gaussian. The convolution of the Gaussian-like instrumental function to the GML distribution is not analytically tractable. The use of a look-up table may be a possible extension to consider the instrumental function.

The physics model presented here is not always applicable. A nonthermal velocity distribution caused by different mechanisms may not be analyzed by the GML distribution, e.g., when the wall temperature and the heat source temperature are similar or when emission from the two separate locations with different temperatures are superimposed. Furthermore, the GML distribution is only applicable $\alpha \gtrsim 0.5$, because of the approximation to derive Eq. (7). If the energy dissipation is dominant compared with elastic collisions, another treatment would be necessary. Establishment of the analytical distribution for a strongly dissipative system is left for future work.

ACKNOWLEDGMENTS

This work was supported by the U.S. D.O.E. Contract No. DE-AC05-00OR22725. An anonimous person with the username *vitamin d*, who gave us an essential suggestion in Ref. [34] is also appreciated. Also the author acknowledges fruitful comments from Dr. Maeyama (Nagoya University), Dr. Shiba (University of Tokyo), and Dr. Elliott (ORNL).

APPENDIX: PROBABILISTIC REPRESENTATION OF ELASTIC COLLISIONS

In the main text, the energy change by an elastic collision is modeled by a probabilistic form Eq. (1). In this Appendix, the details of the assumptions, necessary conditions, as well as the actual form for some particular cases are presented.

1. Necessary condition for a valid $p(x, y)$

The form of $p(x, y)$ in Eq. (1) should depend on the interparticle interaction. Although in the next subsection a particular case (hard-sphere collision) will be discussed, here let us consider the necessary condition for a valid $p(x, y)$.

First, as we consider the elastic collision, the sum of the kinetic energies should be conserved, i.e., $E_1 + E_2 = E_1' + E_2'$, where E_2' is the postcollision energy of particle 2. A similar relation for particle 2 is

$$E_2' \leftarrow (1-y)E_2 + (1-x)E_1. \tag{A1}$$

The exchange of particles 1 and 2 gives the following symmetry condition:

$$p(x, y) = p(1-y, 1-x), \tag{A2}$$

which directly leads to

$$\int_0^1 (x+y)p(x, y)dx\,dy = \int_0^1 p(x, y)dx\,dy = 1. \tag{A3}$$

Find that Eq. (6) reduces to the above equation when substituting $\alpha = 1$ and $\xi = 0$.

Second, the reverse reaction should have the same probability, i.e., $p(x, y)$ should satisfy the detailed balance. Let us consider the two variables $z \equiv E_1/(E_1 + E_2)$ and $z' \equiv E_1'/(E_1' + E_2')$. The conditional probability distribution of z' with given z is

$$p(z'|z) = \frac{1}{z}\int_{\max(0, \frac{z'-z}{1-z})}^{\min(1, \frac{z'}{1-z})} p\left(\frac{z'}{z} - \frac{1-z}{z}y,\, y\right)dy. \tag{A4}$$

The detailed balance can be written as

$$p(z'|z)B\left(z\,\middle|\,\frac{D}{2}, \frac{D}{2}\right) = p(z|z')B\left(z'\,\middle|\,\frac{D}{2}, \frac{D}{2}\right). \tag{A5}$$

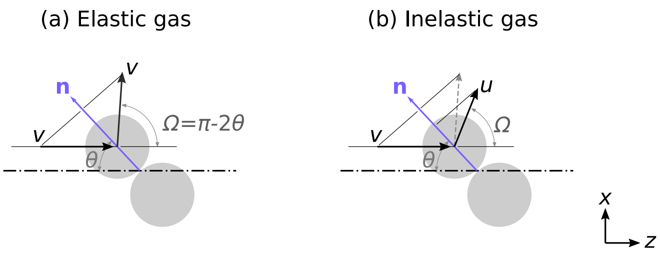

FIG. 13. Schematic illustration of the two-body collision in the center-of-mass frame. (a) Elastic collision and (b) inelastic collision.

$p(x, y)$ should satisfy Eq. (A5) for any pair of z and z'. Note that the beta distribution $B(z|D/2, D/2)$ represents the statistical weight of z in the D-dimensional space. The diffuse collision Eq. (2) and the p-q model, which we will discuss below, satisfy this detailed balance relation.

2. Exact description of elastic collision of hard spheres

Let us consider an elastic collision among two hard spheres having mass 1 [Fig. 13(a)]. Before the collision, two hard spheres have velocities $\mathbf{v}_1$ and $\mathbf{v}_2$. The center-of-mass (c.m.) velocity and their relative velocity is

$$\mathbf{V}_{\text{c.m.}} = \frac{\mathbf{v}_1 + \mathbf{v}_2}{2}, \tag{A6}$$

$$\mathbf{v} = \frac{\mathbf{v}_1 - \mathbf{v}_2}{2}, \tag{A7}$$

respectively. Let Ω be the scattering angle in the center-of-mass frame. The postcollision velocity of the particle 1, $\mathbf{v}_1'$, has the following relation with the precollision velocities,

$$v \equiv |\mathbf{v}_1' - \mathbf{V}_{\text{c.m.}}| = |\mathbf{v}_1 - \mathbf{V}_{\text{c.m.}}|, \tag{A8}$$

$$(\mathbf{v}_1' - \mathbf{V}_{\text{c.m.}}) \cdot (\mathbf{v}_1 - \mathbf{V}_{\text{c.m.}}) = v\cos\Omega. \tag{A9}$$

After a simple equating, we obtain the following relation between the precollision energies E_1, E_2 and postcollision energy E_1',

$$E_1' = \tfrac{1}{2}[(E_1 + E_2) - (E_2 - E_1)\cos\Omega - 2\sqrt{E_1 E_2}\, r \sin\Psi \sin\Omega], \tag{A10}$$

where Ψ is the angle between $\mathbf{v}_1$ and $\mathbf{v}_2$, r is the cosine angle between $\mathbf{V}_{\text{c.m.}}$ and the plane spanned by $\mathbf{v}_{\text{rel}}$ and $\mathbf{v}_{\text{rel}}'$; $\Omega = \pi - 2\theta$, Ψ, and r are independent of each other and they follow

$$\cos^2\theta \sim B\left(\frac{1}{2}, \frac{D-1}{2}\right), \tag{A11}$$

$$\cos^2\Psi \sim B\left(\frac{1}{2}, \frac{D-1}{2}\right), \tag{A12}$$

$$r^2 \sim B\left(\frac{1}{2}, \frac{D-2}{2}\right). \tag{A13}$$

Figure 14 (a) shows the probability distribution of $p(E_1')$ for $D = 3$ case. For comparison, the distribution by Eq. (2) is shown in Fig. 14(b), which has been employed to study gas kinetics for a long time. Despite a small correlation in Fig. 14(a), the overall distribution is similar to the diffuse model.

3. The *p*-*q* model for elastic collision

To capture the correlation found in the exact $p(E_1')$, so-called p-q model has been proposed [17,19]. This model is equivalent to the following probabilistic process:

$$E_1' = (1 - a)E_1 + (aE_1 + bE_2)c, \tag{A14}$$

where a, b, and c are the independent random variables, following

$$a \sim B\left(a \middle| \frac{\gamma}{2}, \frac{D-\gamma}{2}\right), \tag{A15}$$

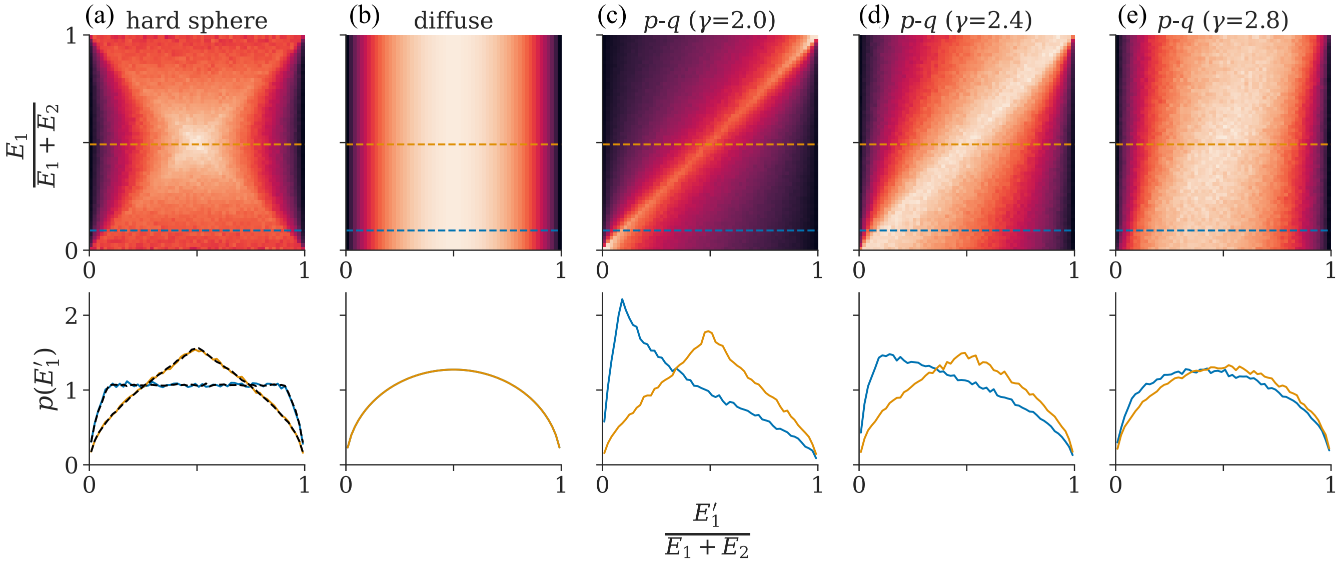

FIG. 14. Probability distribution of the precollision energy E_1 and the postcollision energy E_1'. The lower panel shows the cross sections at the two E_1' values (at the position of the horizon lines in the upper panel). (a) The exact distribution for the hard-sphere collision, (b) the diffuse collision model Eq. (2), and [(c)–(e)] the distribution by p-q model with some values of γ. The dotted curves in the lower panel of (a) show the best fit of the exact distribution by Eq. (A19).

$$b \sim B\left(b\middle|\frac{\gamma}{2},\frac{D-\gamma}{2}\right), \tag{A16}$$

$$c \sim B\left(c\middle|\frac{\gamma}{2},\frac{\gamma}{2}\right), \tag{A17}$$

where $0 \leqslant \gamma \leqslant D$ is a constant that controls the strength of the correlation. Figures 14(c)–14(e) show the distribution of $p(E_1')$ for several values of γ. Depending on the value of γ, $p(E_1')$ changes from a strong memory collision (with small γ) to a nearly diffuse collision (with large γ).

Equation (A14) has the form of Eq. (1), where

$$\begin{aligned} p(x,y|\gamma) = {} & \frac{(1-x)^{\gamma/2-1}y^{\gamma/2-1}}{B\left(\frac{\gamma}{2},\frac{\gamma}{2}\right)\left[B\left(\frac{\gamma}{2},\frac{D-\gamma}{2}\right)\right]^2}\int_y^x c^{(\gamma-D)/2-2} \\ & \times (1-c)^{(\gamma-D)/2-2}(x-c)^{(D-\gamma)/2-1} \\ & \times (c-y)^{(D-\gamma)/2-1}dc. \end{aligned} \tag{A18}$$

It can be easily shown that this $p(x,y|\gamma)$ with any value of γ is a valid probability distribution that leads the Maxwell distribution in the steady state when used in Eq. (3). Similarly, $p(y,x|\gamma)$ is also a valid distribution. Furthermore, the mixture of $p(x,y|\gamma)$ and $p(y,x|\gamma)$ for different values of γ is also valid, which is the linear superposition of $p(x,y|\gamma)$ and $p(y,x|\gamma)$ with arbitrary weight distributions $p_1(\gamma)$ and $p_2(\gamma)$,

$$\begin{aligned} p(x,y) = {} & \eta\int_0^D p(x,y|\gamma)p_1(\gamma)d\gamma \\ & + (1-\eta)\int_0^D p(y,x|\gamma)p_2(\gamma)d\gamma. \end{aligned} \tag{A19}$$

Here $0 \leqslant \eta \leqslant 1$ is the relative weight of the two terms. Dotted curves in the lower panel of Fig. 14(a) shows the best fit of the exact kernel $p(x,y)$ [Eq. (A13)] by Eq. (A19). This perfectly represents the exact solution. Because of the flexibility in Eq. (A19), most of the realistic collision can be represented by Eq. (1).

---

[1] S. B. Vrhovac, S. B. Radovanov, S. A. Bzenić, Z. L. Petrović, and B. M. Jelenković, Chem. Phys. **153**, 233 (1991).

[2] J. Amorim, G. Baravian, and J. Jolly, J. Phys. D **33**, R51 (2000).

[3] U. Samm, P. Bogen, H. Hartwig, E. Hintz, K. Höthker, Y. T. Lie, A. Pospieszczyk, D. Rusbüldt, B. Schweer, and Y. J. Yu, J. Nucl. Mater. **162-164**, 24 (1989).

[4] J. D. Hey, C. C. Chu, and E. Hintz, J. Phys. B: At. Mol. Opt. Phys. **32**, 3555 (1999).

[5] T. Shikama, S. Kado, H. Zushi, A. Iwamae, and S. Tanaka, Phys. Plasmas **11**, 4701 (2004).

[6] K. Sasaki, Y. Okumura, and R. Asaoka, Int. J. Spectrosc. **2010**, 627571 (2009).

[7] S. J. B. Corrigan, J. Chem. Phys. **43**, 4381 (1965).

[8] J. D. Hey, C. C. Chu, P. Mertens, S. Brezinsek, and B. Unterberg, J. Phys. B: At. Mol. Opt. Phys. **37**, 2543 (2004).

[9] L. H. Scarlett, J. K. Tapley, D. V. Fursa, M. C. Zammit, J. S. Savage, and I. Bray, Phys. Rev. A **96**, 062708 (2017).

[10] J. W. McConkey, C. P. Malone, P. V. Johnson, C. Winstead, V. McKoy, and I. Kanik, Phys. Rep. **466**, 1 (2008).

[11] A. Y. Starikovskiy, Philos. Trans. R. Soc. A **373**, 20140343 (2015).

[12] T. J. Sommerer and M. J. Kushner, J. Appl. Phys. **70**, 1240 (1991).

[13] A. A. Ponomarev and N. L. Aleksandrov, Plasma Sources Sci. Technol. **26**, 044003 (2017).

[14] E. Ben-Naim and J. Machta, Phys. Rev. Lett. **94**, 138001 (2005).

[15] E. Ben-Naim, B. Machta, and J. Machta, Phys. Rev. E **72**, 021302 (2005).

[16] W. Kang, J. Machta, and E. Ben-Naim, Europhys. Lett. **91**, 34002 (2010).

[17] E. J. Futcher and M. R. Hoare, Phys. Lett. A **75**, 443 (1980).

[18] E. M. Hendriks and M. H. Ernst, Physica A **112**, 119 (1982).

[19] E. J. Futcher and M. R. Hoare, Physica A **122**, 516 (1983).

[20] H. J. Haubold, A. M. Mathai, and R. K. Saxena, J. Appl. Math. **2011**, 298628 (2011).

[21] L. Barabesi, A. Cerasa, A. Cerioli, and D. Perrotta, Eur. J. Sport Sci. **10**, 3871 (2016).

[22] V. Korolev, A. Gorshenin, and A. Zeifman, J. Math. Sci. **246**, 503 (2020).

[23] H. S. W. Massey, Proc. R. Soc. Lond. A **144**, 188 (1934).

[24] M. Flannery, in *Springer Handbook of Atomic, Molecular, and Optical Physics*, edited by G. Drake (Springer, New York, 2006), pp. 659–691.

[25] N. V. Brilliantov and T. Pöschel, *Kinetic Theory of Granular Gases*, Oxford Graduate Texts (Oxford University Press, Oxford, 2004).

[26] I. S. Aranson and L. S. Tsimring, Rev. Mod. Phys. **78**, 641 (2006).

[27] T. Tabata, R. Ito, Y. Itikawa, N. Itoh, and K. Morita, Atomic Data and Nuclear Data Tables **28**, 493 (1983).

[28] A. P. Thompson, H. M. Aktulga, R. Berger, D. S. Bolintineanu, W. M. Brown, P. S. Crozier, P. J. in 't Veld, A. Kohlmeyer, S. G. Moore, T. D. Nguyen, R. Shan, M. J. Stevens, J. Tranchida, C. Trott, and S. J. Plimpton, Comput. Phys. Commun. **271**, 108171 (2022).

[29] E. M. Baroody, Phys. Fluids **4**, 1182 (1961).

[30] J. Amorim, G. Baravian, and G. Sultan, Appl. Phys. Lett. **68**, 1915 (1996).

[31] NSO's historical archive, https://nso.edu/data/historical-archive/.

[32] *International Atomic Energy Agency, Atomic and Plasma Material Interaction Data for Fusion*, Vol. 8 (IAEA, Vienna, 1999).

[33] T. K. Mankodi, U. V. Bhandarkar, and R. S. E. Myong, Phys. Fluids **32**, 036102 (2020).

[34] https://mathoverflow.net/questions/401835/.